NANO LETTERS

pubs.acs.org/NanoLett Letter

Ultrafast Carrier–Lattice Interactions and Interlayer Modulations of Bi_2Se_3 by X-ray Free-Electron Laser Diffraction

Sungwon Kim, Youngsam Kim, Jaeseung Kim, Sungwook Choi, Kyuseok Yun, Dongjin Kim, Soo Yeon Lim, Sunam Kim, Sae Hwan Chun, Jaeku Park, Intae Eom, Kyung Sook Kim, Tae-Yeong Koo, Yunbo Ou, Ferhat Katmis, Haidan Wen, Anthony DiChiara, Donald A. Walko, Eric C. Landahl, Hyeonsik Cheong, Eunji Sim, Jagadeesh Moodera, and Hyunjung Kim*

Cite This: *Nano Lett.* 2021, 21, 8554–8562 Read Online

ACCESS | Metrics & More | Article Recommendations | Supporting Information

ABSTRACT: As a 3D topological insulator, bismuth selenide (Bi_2Se_3) has potential applications for electrically and optically controllable magnetic and optoelectronic devices. Understanding the coupling with its topological phase requires studying the interactions of carriers with the lattice on time scales down to the subpicosecond regime. Here, we investigate the ultrafast carrier-induced lattice contractions and interlayer modulations in Bi_2Se_3 thin films by time-resolved diffraction using an X-ray free-electron laser. The lattice contraction depends on the carrier concentration and is followed by an interlayer expansion accompanied by oscillations. Using density functional theory and the Lifshitz model, the initial contraction can be explained by van der Waals force modulation of the confined free carrier layers. Our theoretical calculations suggest that the band inversion, related to a topological phase transition, is modulated by the expansion of the interlayer distance. These results provide insights into the topological phase control by light-induced structural change on ultrafast time scales.

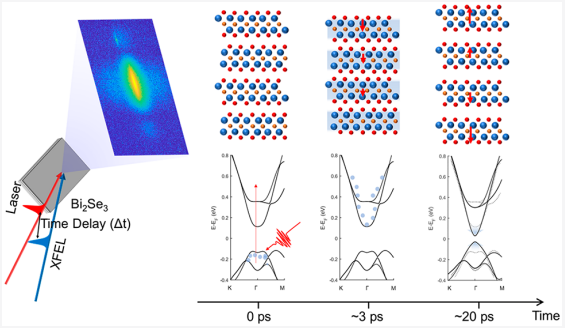

KEYWORDS: *Ultrafast X-ray diffraction, X-ray free-electron laser, bismuth selenide, carrier–lattice interaction, topological insulator, band inversion*

Bismuth selenide (Bi_2Se_3) is a well-known thermoelectric material,[1,2] a V–VI semiconductor, and 2D van der Waals (vdW) material[3] consisting of quintuple layers (QLs). As a 3D topological insulator,[4−7] Bi_2Se_3 has potential applications in optoelectronic[8,9] and electronic devices[4,6,10−13] and has been extensively studied. Furthermore, new applications have been suggested for heterostructures with strong spin–orbit coupling and spin–momentum locking.[14] It is therefore important to study ultrafast carrier-related intra- and interlayer changes in the structure to manipulate the carriers in a topologically nontrivial, quasi-2D-layered system.[11−13,15−17]

Time-and-angle-resolved photoemission spectroscopy (trARPES) was used to study the relaxation dynamics of optically excited carriers decaying through the surface state (SS),[18] as well as oscillatory modulations of the electronic structure in the bulk and SSs.[19] Using transient laser reflections, longitudinal optical (LO) phonons with measurable carrier relaxation times were observed during electron–LO–phonon scattering.[20] These observations revealed a carrier relaxation mechanism representing a hybrid between one dominated by bulk polar phonon interactions and one dominated by surface electron–lattice interactions. How the Bi_2Se_3 carrier–lattice interactions couple with the vdW structures, however, needs to be investigated by direct observations. Using an X-ray free-electron laser (XFEL),[21−26] atomic-scale lattice movements and distortions can be measured directly on a time scale of a few tens of femtoseconds.

Here, we show the ultrafast carrier-induced dynamics of the Bi_2Se_3 lattice studied by ultrafast time-resolved X-ray diffraction (UTXRD). The excited carriers induced a lattice contraction that lasted up to 10 ps. Due to a confined layer of free carriers, high laser fluence may saturate the contraction. The contraction was followed by a lattice expansion that lasted tens of picoseconds and interlayer vibrations with breathing and interface modes. The vibrations were caused by

Received: April 11, 2021
Revised: September 13, 2021
Published: October 8, 2021

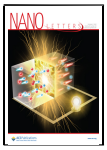

https://doi.org/10.1021/acs.nanolett.1c01424
Nano Lett. 2021, 21, 8554–8562

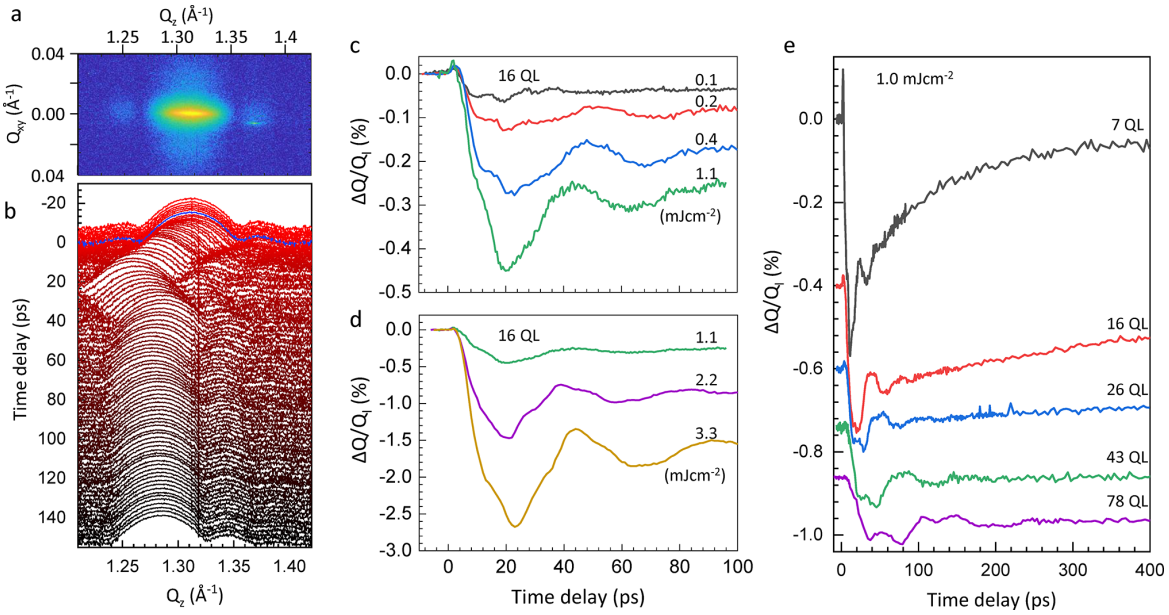

Figure 1. Strain evolution observed at the (006) Bragg peak. (a) The (006) Bragg reflection before laser excitation. (b) The mean intensity of the (006) Bragg peak in the range of 0.08 Å^{-1} along Q_{xy} after the time delay. The intensity profile at Δt = 0 is marked by the blue line. (c,d) Strain evolution in a 16 QL Bi_2Se_3 film for different laser fluences. Contractive strains are observed between time delays of 0 and 6 ps. The lattice is subsequently released, and the strain rapidly turns expansive and is accompanied by oscillations. The strain evolution for the low fluences (≤1.1 mJ cm^{-2} in c) and the high fluences (≥1.1 mJ cm^{-2} in d) are shown in a different scale to show the amplitudes clearly. (e) Strain evolution in Bi_2Se_3 films with 7, 16, 26, 43, and 78 QLs at 1.0 mJ cm^{-2} fluence.

modulating vdW forces restoring the out-of-plane distortions. The carrier-induced vdW contraction was explained by density functional theory (DFT) calculations employing the Lifshitz model. We predict that an expansion in the interlayer distance will be followed by an inversion in the topologically nontrivial band state.

With a 500 fs time resolution and delays up to hundreds of picoseconds, the UTXRD measurements were carried out at the X-ray scattering and spectroscopy (XSS) beamline at PAL-XFEL (Pohang, Korea).[27,28] X-ray pulses with a duration of ∼20 fs were used to probe the sample at a time Δt after an optical laser pump pulse. The bandwidth was $\Delta E/E \sim 1.6 \times 10^{-4}$ at 9.7 keV and was provided by a Si(111) double crystal monochromator. The X-ray pulses were focused by beryllium compound refractive lenses (CRL) to a spot of size 20 × 20 μm^2 full width at half-maximum (fwhm) at the sample location. A Ti:sapphire laser with an 800 nm wavelength and pulse width of 100 fs fwhm was used as the optical pump. It was p-polarized to the sample surface, and its angle of incidence was 9.6° (i.e., larger than the X-ray incidence angle). The laser provided effective fluences between 0.1 and 3.3 mJ cm^{-2} on the sample surface. After a time delay of Δt, measurements were taken with the laser on and off and then compared. The X-ray scattering patterns were recorded by a 2D "multiport charged-coupled device" (MPCCD) with a frame rate of 10−30 Hz.

Figure 1a shows the (006) Bragg reflection, accumulated over 60 shots, of a Bi_2Se_3 sample with 16 QLs. Additional features can be seen, such as fringes in Q_z, due to the sample thickness and diffuse scattering in Q_{xy}. The thicknesses of the samples were determined by X-ray reflectivity and by the fringes (ΔQ_{fringe}) of the (006) Bragg peak (Figure S1). After laser pumping, an XFEL pulse probed the structure after a delay Δt. Figure 1b shows the evolution of the mean intensity of the (006) Bragg peak in the range of 0.08 Å^{-1} along Q_{xy} from Figure 1a. The intensity profile at Δt = 0 is plotted as a blue line. To locate the Bragg peak, the signal of the crystal truncation rods was excluded from the raw data (Figure S2 and Movie S1). The peak position was defined as the center of mass (COM). From this, the strain was calculated by the relation $\Delta Q/Q_I$, where Q_I is the initial COM at negative Δt and ΔQ is its change after Δt. Since no changes were observed in Q_{xy}, Q_I and ΔQ have a dependence only in Q_z. Note that compression is defined by a positive ΔQ. The strain as a function of Δt for a 16 QL sample is shown with fluences of 0.1−1.1 mJ cm^{-2} in the range from 0.04 to −0.5% in $\Delta Q/Q$ in Figure 1c and with 1.1−3.3 mJ cm^{-2} in the range from 0.04 to −3.0% in $\Delta Q/Q$ in Figure 1d. The data with 1.1 mJ cm^{-2} are shown in both for comparison.

Figure 1e shows the time-dependent strain of samples with different thicknesses at a fixed laser fluence of 1.0 mJ cm^{-2}. After laser excitation, a contractive strain was observed. The time to reach maximum contraction depended on the sample thickness and laser fluence. An expansion was then observed, followed by a relaxation with oscillations at different frequencies depending on the sample thickness.

Figure 2a,b shows the changes in position relative to the diffraction geometry (Figure S3) for the (006) and (015) Bragg peaks after the laser excitation. The changes in Q_z show the same time behavior for both (006) and (015), with magnitude for the (006) by a factor of ∼6/5 larger than for the (015) as expected; the changes in Q_{xy} showed no difference (Figure S4). We infer the possibility that a change in the

https://doi.org/10.1021/acs.nanolett.1c01424
Nano Lett. 2021, 21, 8554−8562

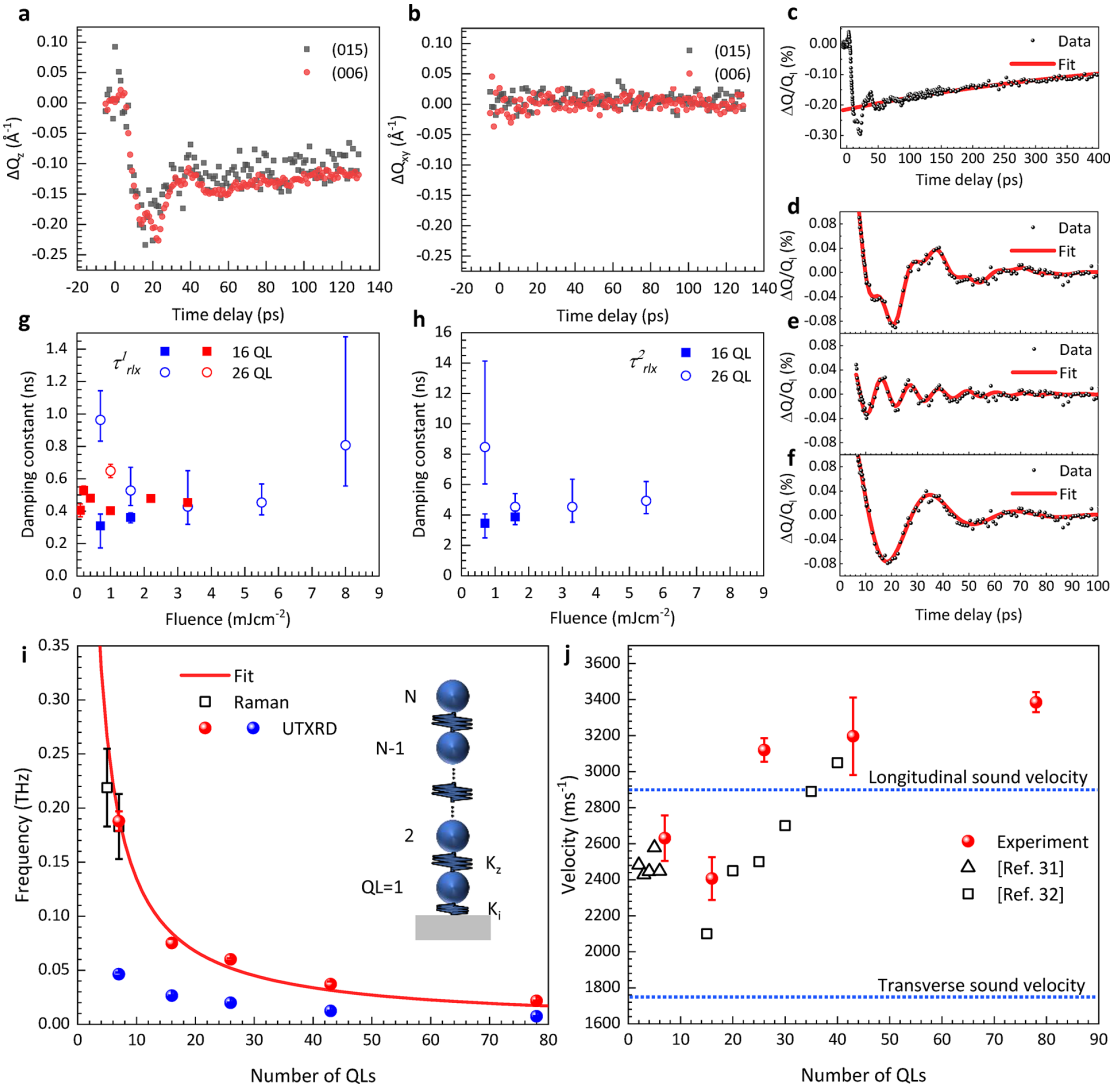

Figure 2. Interlayer vibration modes and relaxation fits to strain curves. (a,b) Position change of the (006) and (015) Bragg peaks in the Q_z and Q_{xy} directions. (c–f) Example of the steps in a strain-curve fitting with a 16 QL sample and 1.0 mJ cm^{-2} fluence; see text for details. (g) Relaxation damping constant τ^1_{rlx} for 16 QL (closed squares) and 26 QL (open circles). The red and blue symbols correspond to the values derived from data obtained at XFEL and the synchrotron source, respectively. (h) τ^2_{rlx} for 16 QL (squares) and 26 QL (circles) derived from data obtained at the synchrotron. (i) Oscillation frequencies for the breathing (red) and interface (blue) modes for Bi_2Se_3 films with different thicknesses. The error bars denote the 95% confidence intervals. The measured Raman frequencies are plotted as squares. The solid red line represents the fit to the breathing mode model. (j) Propagation velocities for the breathing mode are plotted as blue circles. The error bars denote the 95% confidence intervals. The triangle and square represent the measurements obtained by Raman spectroscopy (ref 31) and ultrafast laser reflection (ref 32), respectively.

interlayer distance plays a dominant role in the out-of-plane dynamics.

The oscillations and relaxations are modeled by

$$f_{fit} = \sum_{i=1}^{m} [A^i_{osc} e^{-t/\tau^i_{osc}} \cos 2\pi f^i_{osc}(t - \phi_i)] + \sum_{j=1}^{l} A^j_{rlx} e^{-t/\tau^j_{rlx}} \quad (1)$$

where A_{osc}, τ_{osc}, and f_{osc} are the amplitude, damping constant, and oscillation frequency for the ith component, respectively. A_{rlx} and τ_{rlx} are the relaxation amplitude and damping constant for the jth component, respectively. Figure 2c–f shows the detailed fitting procedures and results for a 16 QL sample with 1.0 mJ cm^{-2} laser fluence. Over the entire time range $\Delta t < 400$ ps, we fit a single exponential relaxation term ($l = 1$, Figure 2c). After subtracting this term, two superposed damping oscillations (Figure 2d) with high ($i = 1$, Figure 2e) and low ($i = 2$, Figure 2f) frequencies were analyzed. For an extended range of Δt, additional damping constants are needed to model the strain relaxation. Figure 2g,h shows the damping constants τ^1_{rlx} and τ^2_{rlx} for both 16 and 26 QL samples, respectively. The error bars represent the 95% confidence intervals. For $\Delta t <$ 1000 ps and the 16 QL sample, the average τ^1_{rlx} is 336 ± 36 ps. However, for $\Delta t > 1.5$ ns, that is, when the coherent motion of

https://doi.org/10.1021/acs.nanolett.1c01424
Nano Lett. 2021, 21, 8554–8562

the lattice diminished and thermal processes dominated, an additional damping constant, $\tau_{rlx}^2 = 3.66 \pm 0.29$ ns, is required. The results do not change significantly with fluence (Figure S5a). The damping constants for the 26 QL sample are greater than those for the 16 QL sample, implying that thermal diffusion takes longer through the thicker sample. Results for other sample thicknesses are provided in the Supporting Information (Figure S5b).

In a plot of the oscillation frequencies, Figure 2i shows two distinct components: a high frequency (red) and a low frequency (blue). The measurements obtained by circularly polarized Raman spectroscopy (squares) are compared to those obtained by fitting a simple linear chain (SLC) model (line). We measured Raman spectra with circular polarization to distinguish out-of-plane and in-plane components without any mixing features. Detailed selection rules for A_{1g} and E_g phonon modes by circular polarized Raman spectroscopy are explained in the Supporting Information. Figures S6 and S7 show all four phonon modes (^1E_g, ^2E_g, ^1A_g, and ^2A_g) and compares the relevant breathing and shear modes with the SLC model. The high-frequency mode is taken as the lowest frequency interlayer breathing mode in an SLC model (Figure 2i, inset). For out-of-plane motions, the QLs (spheres) are bonded together by vdW forces with elastic constant K_z. The force constant between the QLs and the substrate is K_i. Since $K_i \ll K_z$ for the 2D materials on the substrates,[29,30] the eigenmode frequencies can be written as

$$\omega_\alpha \cong \sqrt{\frac{K}{2\mu\pi^2 c^2}\left[1 - \cos\left(\frac{(\alpha - 1)\pi}{N}\right)\right]} \quad (2)$$

where $\alpha = 1$ corresponds to the zero-frequency acoustic mode, and $\alpha = 2, ..., N$ to the interlayer breathing modes when $K = K_z$. The constant c is the speed of light, and μ is 7.5×10^{-6} kg m^{-2} for a single QL of Bi_2Se_3. Fitting eq 2 to the data in Figure 2i gives $K_z = 5.48 \times 10^{19}$ Nm^{-3} for the breathing mode. The breathing mode frequencies obtained from UTXRD and Raman spectroscopy are quantitatively compared to the SLC model in Table S1 in the Supporting Information. Although $\alpha = 2$ was taken as the lowest order of the breathing modes, the low-frequency mode does not resemble the breathing or shearing modes expected in interlayer vibrations. We call this the interface mode for the following reason. Since our UTXRD measurements are sensitive to out-of-plane motions, this mode presumably represents the sample density fluctuations caused by acoustic waves at the sample−substrate interface, subjected to strong interlayer bonding ($K_z \gg K_i$). For each sample thickness, $K_i = 4(\pi c\omega_i)^2 N\mu$. The calculated ($K_i/K_z$) ratios shown in Table 1 are comparable to those for Bi_2Te_3.[31] In principle, the interface modes can be observed in the Raman measurement but could not be observed because the Raman shifts for the interface modes of Bi_2Se_3 are too small. In Figure 2j, the acoustic sound velocities calculated for the breathing mode are compared to the values obtained by Raman measurement[31] (triangles), transient laser reflection[32] (squares), and the longitudinal and transverse values (lines) calculated for the bulk.[33] Our results, showing a dependency on film thickness, are consistent with those in ref 32. This could be due to the coupling of the oscillations (breathing mode) and shear components with the boundary conditions.[32]

Table 1. K_i Values Obtained from the Results with a Simple Linear Chain Model with a Nonzero Substrate Force Constant and K_i/K_z Ratios

thickness (QLs)	7	16	26	43	78
K_i ($\times 10^{18}$ Nm^{-3})	4.35	3.26	2.98	1.90	1.24
K_i/K_z ($\times 10^{-2}$)	8.43	7.67	4.18	2.54	1.48

Figure 3a shows the fluence-dependent contractive strain curves ($\Delta t < 8$ ps) for the 16 QL sample described in Figure 1c,d. The contractive strain data (dots) are shown with fitted error functions (lines). The maximum compression (squares) and corresponding Δt (open circles) are also shown. At a fluence of ~0.4 mJ cm^{-2}, the contraction saturates at $\Delta Q/Q_I \sim$ 0.027% but is tapered during the interval Δt. In this region, we did not observe intralayer LO optical phonon modes at 2.19 THz[20] due to the limitation of the time resolution of our experiment. In addition, the decay time constants for LO phonons are between 1.5 ps (6 nm film) and 3.11 ps (40 nm)[20] with the same laser excitation energy as we used. Therefore, it is difficult to extract the modulation near the peak. After contraction, the expansion reaches a maximum at ~20 ps, independent of the fluence. Figure 3b shows the maximum expansive strain as a function of fluence for the same 16 QL sample. The inset shows an enlarged range of up to 0.5 mJ cm^{-2}. Unlike compression, the expansion is linearly related to the fluence and does not saturate.

To understand how the initial compressive strain is related to the fluence-dependent carrier density (n), we calculated the latter by measuring the transmittance and reflectance values (see Supporting Information). To determine how fluence affects the contraction time, we compared our results with those obtained in a study using trARPES[18] and an 800 nm fs laser for excitation. A 26 μJ cm^{-2} fluence corresponds to 0.1 mJ cm^{-2} (24 μJ cm^{-2} absorbed fluence, after considering transmittance and reflectance) in our measurement. Figure 3c shows the strain curve of fluence of 0.1 mJ cm^{-2}. The 2.47 ps taken to reach maximum contraction is in good agreement with the 2.5 ps[18] taken for the carriers to completely relax by scattering from the higher-lying states after they populated the SS and bulk conduction band (BCB) within 0.7 ps of excitation. Since the X-ray penetrates the entire 16 QLs, the SS population is negligible. The observed contractions are therefore attributed to the carriers that populated the BCB. We estimated the proportionality of the time-dependent BCB population depending on the fluences by the double Gaussian fit of the BCB population shown in Figure 1a [black line (3)] of ref 18. The fluence-dependent contractive impulse can be obtained by integrating the square root of the BCB population using the absorbed fluence. The maximum contraction value increases as the fluence increases before the saturation is reached. For fluences above that needed to saturate the contraction, the time to reach the saturation is reduced with increasing fluence.

To relate the density of the excited carriers to the magnitude of the lattice contraction, we used the Lifshitz model.[34] By considering the dielectric function, this model explains the vdW force between metallic surfaces separated by distance (l), which is small compared to the wavelengths of the fluctuating field. We note that a carrier slab can be retained for several picoseconds after laser excitation due to the anisotropy in electric transport[35] and the formation of a cylindrical Fermi surface.[36,37] The vdW gap might not be entirely insulating, but the conductivity along the stacking direction of QLs is significantly smaller than the conductivity in the basal plane

https://doi.org/10.1021/acs.nanolett.1c01424
Nano Lett. 2021, 21, 8554−8562

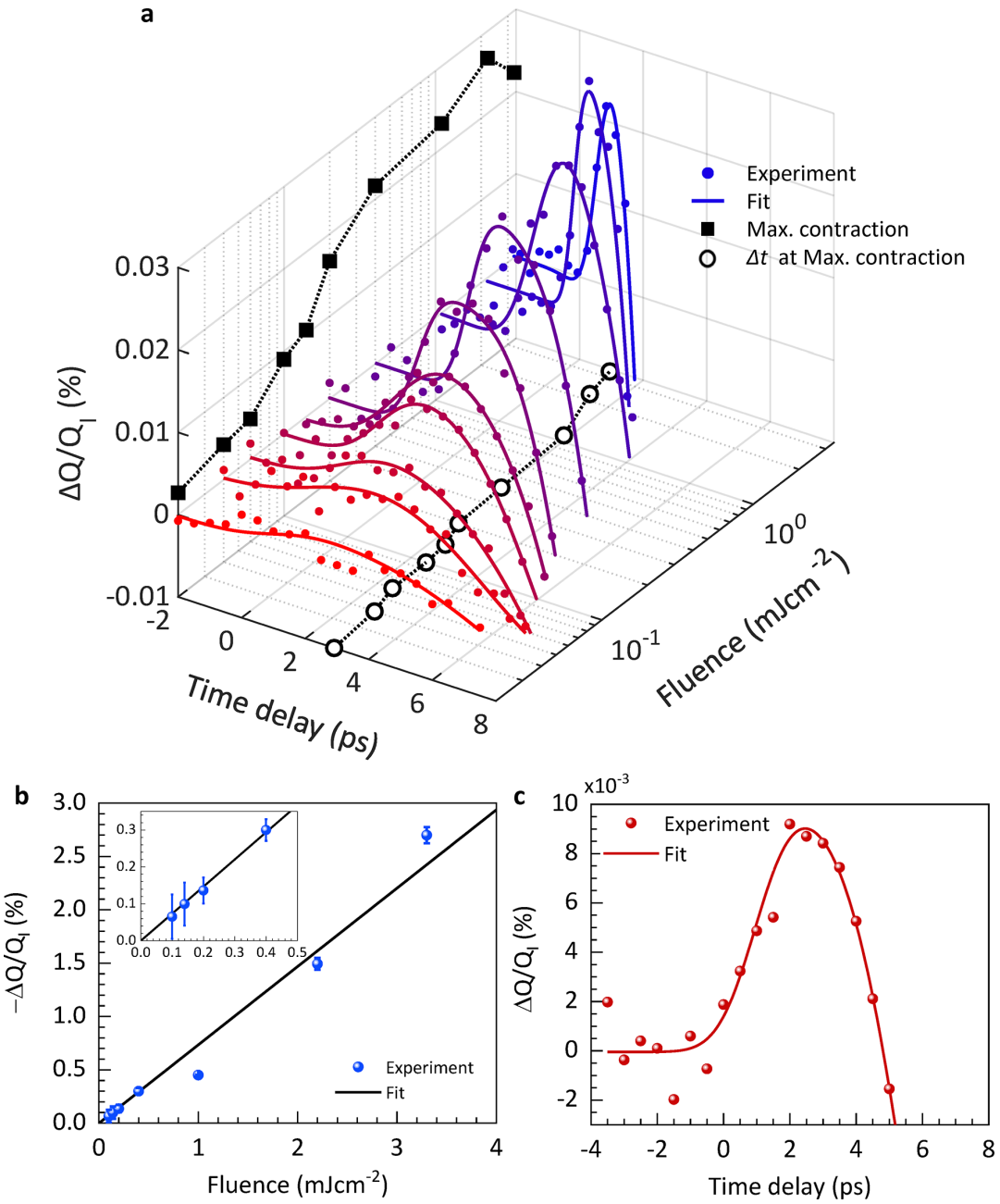

Figure 3. Interlayer contractive strain and maximum expansive strain on a 16 QL Bi_2Se_3 sample. (a) Contractive strain for different fluences up to time delay of 8 ps. The data points (dots) are plotted with the error functions (lines). The maximum contractive strains and their corresponding time delays are plotted as squares and open circles, respectively. (b) Maximum expansive strain as a function of laser fluence for the 16 QL sample from Figure 1c,d. The laser fluence ranges from 0.1 to 3.3 mJ cm^{-2}. The maximum lattice expansion scales linearly with fluence. The maximum expansive strains were taken as the minima in the strain curves. For each time delay, the center of mass is averaged over the measurements, and the error bars represent the standard deviation. (c) Compressive strain as a function of time delay for 1 mJ cm^{-2} fluence. The maximum contraction occurred at a time delay of 2.47 ps.

for bismuth chalcogenides.[35] The anisotropy in conductivity might suppress carrier diffusion crossover vdW gap compared to in-plane. With increasing carrier concentrations of Bi_2Se_3, the anisotropy of the electrical conductivity increases, i.e., transport in the basal plane becomes even more preferential due to the cylindrical change in the Fermi surface since electrons on the Fermi surface are generally responsible for transport phenomena.[36,37]

Therefore, we assume that the excited carriers formed a charge slab inside the QL, and each slab is separated by the distance *l*. At the high carrier density limit, where the plasma frequency is much larger than the Drude damping term in the

https://doi.org/10.1021/acs.nanolett.1c01424
Nano Lett. 2021, 21, 8554−8562

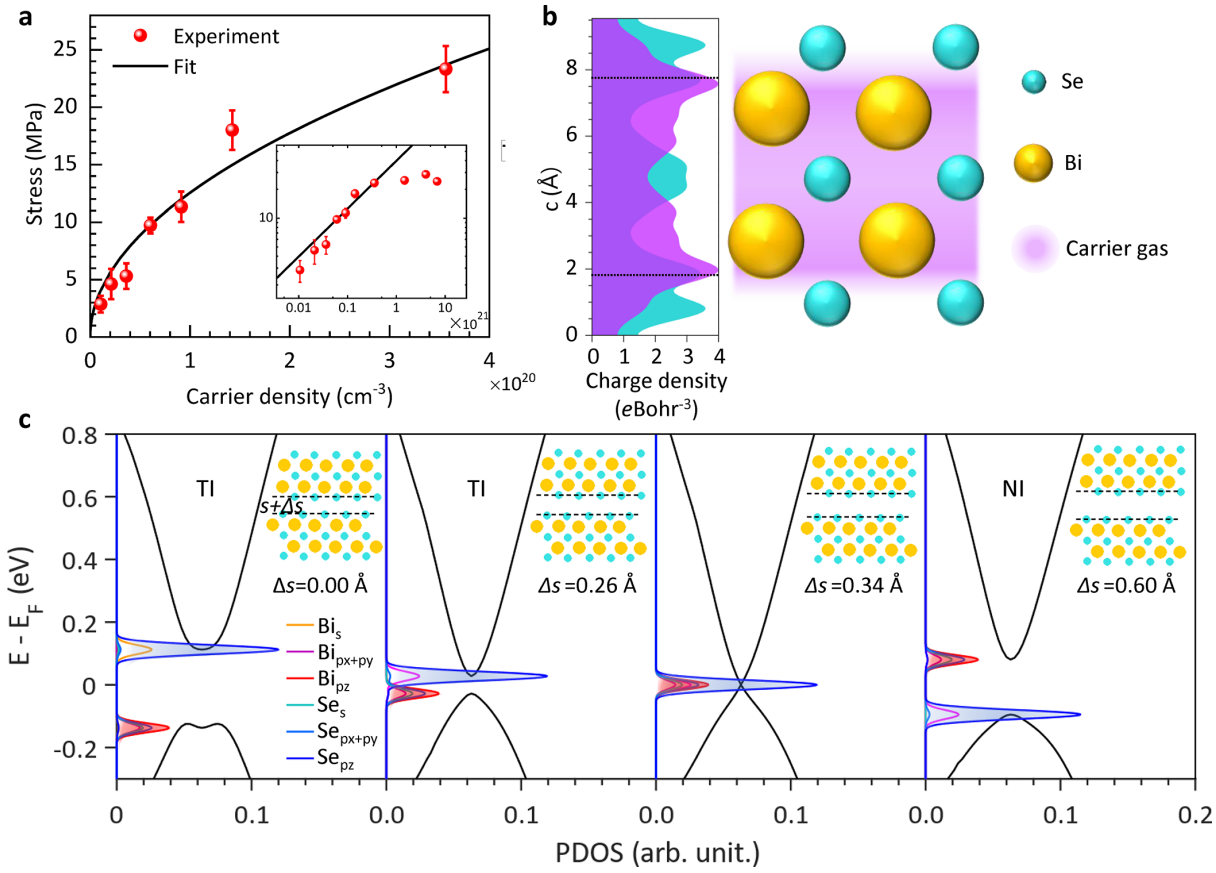

Figure 4. Theoretical analysis of interlayer distance contraction and expansion. (a) Maximum compressive stress is plotted against the carrier density extracted from Figure 3a (red circle), with the Lifshitz model (line) overlaid. The stress data for carrier densities over 3.564×10^{20} (with 0.4 mJ cm^{-2} fluence) were excluded since they were in the saturation regime. The inset shows the entire data set. (b) Calculated charge density (CD) distribution along the *c*-axis of the crystal and the atomic configuration in a QL. To display the carrier distribution, we have aligned the *y*-axis of the CD distribution with the atomic positions. The dashed lines represent the boundaries of the metallic surface in the Lifshitz model. (c) Projected density of states (PDOS) of modulated interlayer distance, **Δ*s***, and the corresponding band structure in the vicinity of the Γ point. The colored lines indicate contributions by atomic orbitals. Band inversion occurs as the interlayer distance expands, resulting in the transition from topological insulator (TI) to normal insulator (NI).

dielectric function, the Drude model gives the effective pressure between charged slabs[26] as

$$\Delta F = \frac{\xi \hbar e \sqrt{n}}{32\pi^2 \sqrt{2m\epsilon_0} l^3} \tag{3}$$

where $\hbar$ is the Planck constant, e is the elementary electron charge, m is the electron mass, ϵ_0 is the vacuum permittivity, n is the carrier density, and $\xi = 2.04$[26] is the Matsubara frequency. The stress is calculated by multiplying the elastic tensor component along the *c*-axis (C_{33}) by the maximum contraction in Figure 3a. Figure 4a shows the compressive stress on the 16 QL sample (circle) as a function of n and the fit with eq 3 (line). The distance l is 3.94 Å from the fit and is larger than the interlayer distance of Bi_2Se_3 (2.58 Å) calculated by DFT. This implies that in Bi_2Se_3, the charge density (CD) within a QL is responsible for the vdW attraction. Note that the data with $n > 3.564 \times 10^{20}$ were excluded from the fit due to saturation (inset of Figure 4a).

After fitting eq 3 to the data, we wanted to explore the meaning of the parameter l in a QL. Using DFT, we calculated the CD of the valence band (VB) and the conduction band (CB). The calculations are described in Supporting Information. Figure 4b shows the CD and atomic configuration in a single QL along the *c*-axis direction. DFT geometry optimization gave the following intralayer distances: 1.58 Å for Se (outer)−Bi, 1.90 Å for Bi−Se (inner), and 2.58 Å for the interlayer distance (s), which is the distance between Se (outer)−Se (outer) layers. The black dashed lines indicate indentations $l/2$ from each edge of the QL (9.55 Å). The CD of the VB (cyan) shows electrons distributed around the Se atoms. The CD of the CB (purple) has a distribution that is diffuse within the dashed lines and decreases sharply outward, reaching a minimum within the interlayer distance. As the region between the dashed lines contains most of the CB carriers (>70%), we consider it as a charged slab with thickness $d = 9.55 - l$ (Å). In other words, the carriers confined within the slab (d) are responsible for the compressive strain.

To investigate how interlayer distance modulation affects the topological phase of Bi_2Se_3,[16,38] we calculated the band structures for different interlayer distances ($s + \Delta s$) while keeping the atomic structure within the QL fixed. The

https://doi.org/10.1021/acs.nanolett.1c01424
Nano Lett. 2021, 21, 8554−8562

calculation is carried out for the ground state without considering the carriers since most carriers are relaxed 20 ps after the laser excitation. In particular, most of the energy relaxation of the excited carriers is completed within 3 ps, after which only the metastable population remains.[18] The exponential attenuation of the laser reflection shows that most of the carriers relax within 10 ps after laser excitation.[32] In addition, the polaron[39] effect can be considered if the electron−phonon coupling is strong enough by the electron overlap assisted by the lattice distortion, which might accompany the broadening of the Bragg peak. In this work, the observed lattice contraction corresponds to MPa of pressure, that is, 3 orders lower than the pressure of several GPa[40] to generate polarons.

The DFT-calculated band structure near the Γ point and corresponding projected density of states (PDOS) with interlayer distance changes (Δs in inset) are overlaid in Figure 4c. The atomic orbitals are indicated by colored lines. The PDOS shows that as Δs expands, p_z orbitals contribute to the inversion state, but the p_z orbital contribution remains constant regardless of inversion. According to our observations, with increasing laser fluence, the lattice expands linearly after the carrier-induced contraction. For a 3.3 mJ cm^{-2} fluence, the out-of-plane lattice parameter expands to 29.43 Å, 0.79 Å larger than the equilibrium state. We attribute most expansion to a coherent interlayer distance modulation since neither significant in-plane lattice change nor evidence of lattice thermalization has been observed on this time scale. In the DFT calculations, the energy gap between the inverted states narrows when the interlayer distance expands. The band is inverted when the interlayer distance expansion exceeds 0.34 Å, predicting a topological phase transition to a normal insulator. Similar dimensional crossover related to the vdW gap was discussed with a maximum of 4% strain generated by external stimuli, that is, mechanical bending force.[35] In this work, the largest observed interlayer distance expansion is 0.26 Å; the corresponding energy band gap is 0.06 eV—a reduction of 0.24 eV compared to the equilibrium state. This suggests that the topological phase is optically tunable on an ultrafast time scale. We carried out additional DFT calculations to estimate the band gap change when the interlayer contraction occurs. As a result, we obtained the band gap changes of 1−2 meV for 0.2 pm contraction (i.e., the maximum value observed in our study) and a conduction band shift of 1−3 meV.

In conclusion, we have studied the lattice dynamics of Bi_2Se_3 on ultrafast time scales, observing the consecutive dynamical phases induced by carrier excitation. During $\Delta t < \sim 6$ ps, due to the presence of a concentrated layer of carriers within a QL, an impulsive contraction is induced by modulating vdW forces. By performing DFT calculations with the Lifshitz model, we found that the carrier layer is 5.61 Å thick, with 70% of the carriers occupying the CB. As the contraction is reversed by carrier−lattice interaction, we observed breathing and interface mode oscillations. The vibration modes of the interlayer oscillations are assigned by an SLC model. The linear relationship between the sample thickness and damping constants of the oscillations and relaxations suggests a role for thermal diffusion. The Bi_2Se_3 samples undergo maximum interlayer expansion at the beginning of the interlayer oscillations. How the topologically inverted states near the Fermi level are modulated is explained quantitatively by the expansion of the interlayer distance. With an expansion of c by 0.26 Å, the bulk band gap is expected to narrow to 0.06 eV. Hence, a topological phase transition to a normal insulator is predicted for an expansion larger than 0.34 Å. We show the possibility to control the interlayer distance by laser excitation, such as light-induced phase control, that can reach the regime of the crossover band gap. These findings may provide insights relevant to applications that utilize the ultrafast topological states in 2D topological insulators.

■ ASSOCIATED CONTENT

Supporting Information

The Supporting Information is available free of charge at https://pubs.acs.org/doi/10.1021/acs.nanolett.1c01424.

Sample preparation, film thickness determination by X-ray reflectivity measurements, reduction of crystal truncation rods, Raman measurement of Bi_2Se_3, exponential relaxations in the extended time delay range, and density functional theory calculations (PDF)

Movie for evolution of (006) Bragg diffraction and its in-plane mean valued profile (ZIP)

■ AUTHOR INFORMATION

Corresponding Author

Hyunjung Kim − *Department of Physics, Sogang University, Seoul 04107, Korea;* orcid.org/0000-0001-6211-4888; Phone: +82 2 705 8431; Email: hkim@sogang.ac.kr

Authors

Sungwon Kim − *Department of Physics, Sogang University, Seoul 04107, Korea;* orcid.org/0000-0001-8035-1721

Youngsam Kim − *Department of Chemistry, Yonsei University, Seoul 03722, Korea;* orcid.org/0000-0001-8020-0130

Jaeseung Kim − *Department of Physics, Sogang University, Seoul 04107, Korea;* orcid.org/0000-0001-5014-6954

Sungwook Choi − *Department of Physics, Sogang University, Seoul 04107, Korea;* orcid.org/0000-0001-9847-8755

Kyuseok Yun − *Department of Physics, Sogang University, Seoul 04107, Korea*

Dongjin Kim − *Department of Physics, Sogang University, Seoul 04107, Korea*

Soo Yeon Lim − *Department of Physics, Sogang University, Seoul 04107, Korea*

Sunam Kim − *Pohang Accelerator Laboratory, Pohang 37673, Korea*

Sae Hwan Chun − *Pohang Accelerator Laboratory, Pohang 37673, Korea*

Jaeku Park − *Pohang Accelerator Laboratory, Pohang 37673, Korea*

Intae Eom − *Pohang Accelerator Laboratory, Pohang 37673, Korea*

Kyung Sook Kim − *Pohang Accelerator Laboratory, Pohang 37673, Korea*

Tae-Yeong Koo − *Pohang Accelerator Laboratory, Pohang 37673, Korea*

Yunbo Ou − *Francis Bitter Magnet Laboratory, Massachusetts Institute of Technology, Cambridge, Massachusetts 02139, United States*

Ferhat Katmis − *Francis Bitter Magnet Laboratory, Massachusetts Institute of Technology, Cambridge, Massachusetts 02139, United States*

https://doi.org/10.1021/acs.nanolett.1c01424
Nano Lett. 2021, 21, 8554−8562

Haidan Wen − *Advanced Photon Source, Argonne National Laboratory, Argonne, Illinois 60439, United States;* orcid.org/0000-0002-5427-175X
Anthony DiChiara − *Advanced Photon Source, Argonne National Laboratory, Argonne, Illinois 60439, United States*
Donald A. Walko − *Advanced Photon Source, Argonne National Laboratory, Argonne, Illinois 60439, United States*
Eric C. Landahl − *Department of Physics, DePaul University, Chicago, Illinois 60614, United States*
Hyeonsik Cheong − *Department of Physics, Sogang University, Seoul 04107, Korea;* orcid.org/0000-0002-2347-4044
Eunji Sim − *Department of Chemistry, Yonsei University, Seoul 03722, Korea;* orcid.org/0000-0002-4139-0960
Jagadeesh Moodera − *Francis Bitter Magnet Laboratory and Department of Physics, Massachusetts Institute of Technology, Cambridge, Massachusetts 02139, United States*

Complete contact information is available at: https://pubs.acs.org/10.1021/acs.nanolett.1c01424

Author Contributions

H.K. supervised and coordinated all aspects of the project. The UTXRD measurements at PAL-XFEL were carried out by S.K., J.K., S.C., K.Y., D.K., S.K., S.H.C., J.P., I.E., K.K., T.-Y.K., and H.K. The UTXRD measurements at APS were carried out by S.K., K.Y., H.W., A.D.D., D.A.W., E.C.L., and H.K. The UTXRD data were analyzed by S.K. The Bi_2Se_3 thin films were grown by Y.O. and F.K. under the supervision of J.S.M. The XRR measurements were carried out by J.K. and S.K. The theoretical analyses and density functional theory calculations were carried out by S.K. and Y.K., under the supervision of E.S. and H.K. S.Y.L. carried out the Raman spectroscopy measurements under the supervision of H.C. S.K., Y.K., E.S., and H.K. wrote the paper. All authors discussed the results and commented on the manuscript.

Notes

The authors declare no competing financial interest.

■ ACKNOWLEDGMENTS

We thank Sanghoon Song and Aymeric Robert for fruitful discussions. This research was supported by the National Research Foundation of Korea (NRF-2015R1A5A1009962, 2019R1A6B2A02100883, and 2021R1A3B1077076). Y.K. and E.S. acknowledge the support from NRF-2020R1A2C2007468. H.W. acknowledges the support of U.S. Department of Energy (DOE), Office of Science, Basic Energy Sciences, Materials Sciences and Engineering Division. This research used resources of the Advanced Photon Source, a U.S. DOE Office of Science User Facility, operated for the DOE Office of Science by Argonne National Laboratory under Contract No. DE-AC02-06CH11357. The experiments were carried out at the XSS beamline of PAL-XFEL (experiment no. 2017-1st-FXS-006 and 2018-1st-XSS-010) funded by the Ministry of Science and ICT of Korea. The work at MIT was supported by the Center for Integrated Quantum Materials (NSF-DMR 1231319), the NSF Grant No. DMR 1700137, NSF CONVERGENCE ACCELERATOR TRACK C: SYN OIA-2040620, and ONR Grant Nos. N00014-16-1-2657 and N00014-20-1-2306.

■ ABBREVIATIONS

Bi_2Se_3, bismuth selenide; vdW, van der Waals; QL, quintuple layer; trARPES, time-angle-resolved photoemission spectroscopy; SS, surface state; LO, longitudinal optical; XFEL, X-ray free-electron laser; UTXRD, ultrafast time-resolved X-ray diffraction; DFT, density functional theory; XSS, X-ray scattering and spectroscopy; CRL, beryllium compound refractive lenses; fwhm, full width at half-maximum; COM, center of mass; SLC, simple linear chain; BCB, bulk conduction band; CD, charge density; VB, valence band; CB, conduction band; PDOS, projected density of state

■ REFERENCES

(1) Mishra, S. K.; Satpathy, S.; Jepsen, O. Electronic Structure and Thermoelectric Properties of Bismuth Telluride and Bismuth Selenide. *J. Phys.: Condens. Matter* **1997**, *9* (2), 461−470.
(2) Ghaemi, P.; Mong, R. S. K.; Moore, J. E. In-Plane Transport and Enhanced Thermoelectric Performance in Thin Films of the Topological Insulators Bi_2Te_3 and Bi $_2Se_3$. *Phys. Rev. Lett.* **2010**, *105* (16), 166603.
(3) Geim, A. K.; Grigorieva, I. V. Van Der Waals Heterostructures. *Nature* **2013**, *499* (7459), 419−425.
(4) Zhang, H.; Liu, C. X.; Qi, X. L.; Dai, X.; Fang, Z.; Zhang, S. C. Topological Insulators in Bi_2Se_3, Bi $_2$ Te $_3$ and Sb_2Te_3 with a Single Dirac Cone on the Surface. *Nat. Phys.* **2009**, *5* (6), 438−442.
(5) Moore, J. E. The Birth of Topological Insulators. *Nature* **2010**, *464* (7286), 194−198.
(6) Qi, X. L.; Zhang, S. C. Topological Insulators and Superconductors. *Rev. Mod. Phys.* **2011**, *83* (4), 1057−1110.
(7) Fu, L.; Kane, C. L.; Mele, E. J. Topological Insulators in Three Dimensions. *Phys. Rev. Lett.* **2007**, *98* (10), 106803.
(8) Zhang, H.; Zhang, X.; Liu, C.; Lee, S. T.; Jie, J. High-Responsivity, High-Detectivity, Ultrafast Topological Insulator Bi_2Se_3/Silicon Heterostructure Broadband Photodetectors. *ACS Nano* **2016**, *10* (5), 5113−5122.
(9) Wang, F.; Li, L.; Huang, W.; Li, L.; Jin, B.; Li, H.; Zhai, T. Submillimeter 2D Bi_2Se_3 Flakes toward High-Performance Infrared Photodetection at Optical Communication Wavelength. *Adv. Funct. Mater.* **2018**, *28* (33), 1−10.
(10) Mellnik, A. R.; Lee, J. S.; Richardella, A.; Grab, J. L.; Mintun, P. J.; Fischer, M. H.; Vaezi, A.; Manchon, A.; Kim, E. A.; Samarth, N.; Ralph, D. C. Spin-Transfer Torque Generated by a Topological Insulator. *Nature* **2014**, *511* (7510), 449−451.
(11) Luo, L.; Yang, X.; Liu, X.; Liu, Z.; Vaswani, C.; Cheng, D.; Mootz, M.; Zhao, X.; Yao, Y.; Wang, C. Z.; Ho, K. M.; Perakis, I. E.; Dobrowolska, M.; Furdyna, J. K.; Wang, J. Ultrafast Manipulation of Topologically Enhanced Surface Transport Driven by Mid-Infrared and Terahertz Pulses in Bi_2Se_3. *Nat. Commun.* **2019**, *10* (1), 607.
(12) Checkelsky, J. G.; Hor, Y. S.; Cava, R. J.; Ong, N. P. Bulk Band Gap and Surface State Conduction Observed in Voltage-Tuned Crystals of the Topological Insulator Bi_2Se_3. *Phys. Rev. Lett.* **2011**, *106* (19), 4−7.
(13) Kim, D.; Cho, S.; Butch, N. P.; Syers, P.; Kirshenbaum, K.; Adam, S.; Paglione, J.; Fuhrer, M. S. Surface Conduction of Topological Dirac Electrons in Bulk Insulating Bi_2 Se_3. *Nat. Phys.* **2012**, *8* (6), 459−463.
(14) Katmis, F.; Lauter, V.; Nogueira, F. S.; Assaf, B. A.; Jamer, M. E.; Wei, P.; Satpati, B.; Freeland, J. W.; Eremin, I.; Heiman, D.; Jarillo-Herrero, P.; Moodera, J. S. A High-Temperature Ferromagnetic Topological Insulating Phase by Proximity Coupling. *Nature* **2016**, *533* (7604), 513−516.
(15) Flötotto, D.; Bai, Y.; Chan, Y. H.; Chen, P.; Wang, X.; Rossi, P.; Xu, C. Z.; Zhang, C.; Hlevyack, J. A.; Denlinger, J. D.; Hong, H.; Chou, M. Y.; Mittemeijer, E. J.; Eckstein, J. N.; Chiang, T. C. In Situ Strain Tuning of the Dirac Surface States in Bi_2Se_3 Films. *Nano Lett.* **2018**, *18* (9), 5628−5632.

(16) Aramberri, H.; Muñoz, M. C. Strain-Driven Tunable Topological States in Bi_2Se_3. *J. Phys. Mater.* **2018**, *1* (1), 015009.
(17) Hsieh, D.; Xia, Y.; Qian, D.; Wray, L.; Dil, J. H.; Meier, F.; Osterwalder, J.; Patthey, L.; Checkelsky, J. G.; Ong, N. P.; Fedorov, A. V.; Lin, H.; Bansil, A.; Grauer, D.; Hor, Y. S.; Cava, R. J.; Hasan, M. Z. A Tunable Topological Insulator in the Spin Helical Dirac Transport Regime. *Nature* **2009**, *460* (7259), 1101−1105.
(18) Sobota, J. A.; Yang, S.; Analytis, J. G.; Chen, Y. L.; Fisher, I. R.; Kirchmann, P. S.; Shen, Z. X. Ultrafast Optical Excitation of a Persistent Surface-State Population in the Topological Insulator Bi_2Se_3. *Phys. Rev. Lett.* **2012**, *108* (11), 117403.
(19) Sobota, J. A.; Yang, S. L.; Leuenberger, D.; Kemper, A. F.; Analytis, J. G.; Fisher, I. R.; Kirchmann, P. S.; Devereaux, T. P.; Shen, Z. X. Distinguishing Bulk and Surface Electron-Phonon Coupling in the Topological Insulator Bi_2Se_3 Using Time-Resolved Photoemission Spectroscopy. *Phys. Rev. Lett.* **2014**, *113* (15), 157401.
(20) Glinka, Y. D.; Babakiray, S.; Johnson, T. A.; Bristow, A. D.; Holcomb, M. B.; Lederman, D. Ultrafast Carrier Dynamics in Thin-Films of the Topological Insulator Bi_2Se_3. *Appl. Phys. Lett.* **2013**, *103* (15), 151903.
(21) Zhu, D.; Robert, A.; Henighan, T.; Lemke, H. T.; Chollet, M.; Glownia, J. M.; Reis, D. A.; Trigo, M. Phonon Spectroscopy with Sub-MeV Resolution by Femtosecond x-Ray Diffuse Scattering. *Phys. Rev. B: Condens. Matter Mater. Phys.* **2015**, *92* (5), 054303−1.
(22) Fritz, D. M. Ultrafast Bond Softening in Bismuth . *Science (80-.)* **2007**, *315*, 633−637.
(23) Trigo, M.; Fuchs, M.; Chen, J.; Jiang, M. P.; Cammarata, M.; Fahy, S.; Fritz, D. M.; Gaffney, K.; Ghimire, S.; Higginbotham, A.; Johnson, S. L.; Kozina, M. E.; Larsson, J.; Lemke, H.; Lindenberg, A. M.; Ndabashimiye, G.; Quirin, F.; Sokolowski-Tinten, K.; Uher, C.; Wang, G.; Wark, J. S.; Zhu, D.; Reis, D. A. Fourier-Transform Inelastic X-Ray Scattering from Time- and Momentum-Dependent Phonon-Phonon Correlations. *Nat. Phys.* **2013**, *9* (12), 790−794.
(24) Zalden, P.; Quirin, F.; Schumacher, M.; Siegel, J.; Wei, S.; Koc, A.; Nicoul, M.; Trigo, M.; Andreasson, P.; Enquist, H.; Shu, M. J.; Pardini, T.; Chollet, M.; Zhu, D.; Lemke, H.; Ronneberger, I.; Larsson, J.; Lindenberg, A. M.; Fischer, H. E.; Hau-Riege, S.; Reis, D. A.; Mazzarello, R.; Wuttig, M.; Sokolowski-Tinten, K. Femtosecond X-Ray Diffraction Reveals a Liquid−Liquid Phase Transition in Phase-Change Materials. *Science (Washington, DC, U. S.)* **2019**, *364* (6445), 1062−1067.
(25) Lindenberg, A. M.; Johnson, S. L.; Reis, D. A. Visualization of Atomic-Scale Motions in Materials via Femtosecond X-Ray Scattering Techniques. *Annu. Rev. Mater. Res.* **2017**, *47* (1), 425−449.
(26) Mannebach, E. M.; Nyby, C.; Ernst, F.; Zhou, Y.; Tolsma, J.; Li, Y.; Sher, M. J.; Tung, I. C.; Zhou, H.; Zhang, Q.; Seyler, K. L.; Clark, G.; Lin, Y.; Zhu, D.; Glownia, J. M.; Kozina, M. E.; Song, S.; Nelson, S.; Mehta, A.; Yu, Y.; Pant, A.; Aslan, O. B.; Raja, A.; Guo, Y.; Dichiara, A.; Mao, W.; Cao, L.; Tongay, S.; Sun, J.; Singh, D. J.; Heinz, T. F.; Xu, X.; Macdonald, A. H.; Reed, E.; Wen, H.; Lindenberg, A. M. Dynamic Optical Tuning of Interlayer Interactions in the Transition Metal Dichalcogenides. *Nano Lett.* **2017**, *17* (12), 7761−7766.
(27) Kang, H. S.; Min, C. K.; Heo, H.; Kim, C.; Yang, H.; Kim, G.; Nam, I.; Baek, S. Y.; Choi, H. J.; Mun, G.; Park, B. R.; Suh, Y. J.; Shin, D. C.; Hu, J.; Hong, J.; Jung, S.; Kim, S. H.; Kim, K. H.; Na, D.; Park, S. S.; Park, Y. J.; Han, J. H.; Jung, Y. G.; Jeong, S. H.; Lee, H. G.; Lee, S.; Lee, S.; Lee, W. W.; Oh, B.; Suh, H. S.; Parc, Y. W.; Park, S. J.; Kim, M. H.; Jung, N. S.; Kim, Y. C.; Lee, M. S.; Lee, B. H.; Sung, C. W.; Mok, I. S.; Yang, J. M.; Lee, C. S.; Shin, H.; Kim, J. H.; Kim, Y.; Lee, J. H.; Park, S. Y.; Kim, J.; Park, J.; Eom, I.; Rah, S.; Kim, S.; Nam, K. H.; Park, J.; Park, J.; Kim, S.; Kwon, S.; Park, S. H.; Kim, K. S.; Hyun, H.; Kim, S. N.; Kim, S.; Hwang, S. M.; Kim, M. J.; Lim, C. Y.; Yu, C. J.; Kim, B. S.; Kang, T. H.; Kim, K. W.; Kim, S. H.; Lee, H. S.; Lee, H. S.; Park, K. H.; Koo, T. Y.; Kim, D. E.; Ko, I. S. Hard X-Ray Free-Electron Laser with Femtosecond-Scale Timing Jitter. *Nat. Photonics* **2017**, *11* (11), 708−713.
(28) Park, J.; Eom, I.; Kang, T. H.; Rah, S.; Nam, K. H.; Park, J.; Kim, S.; Kwon, S.; Park, S. H.; Kim, K. S.; Hyun, H.; Kim, S. N.; Lee, E. H.; Shin, H.; Kim, S.; Kim, M. J.; Shin, H. J.; Ahn, D.; Lim, J.; Yu, C. J.; Song, C.; Kim, H.; Noh, D. Y.; Kang, H. S.; Kim, B.; Kim, K. W.; Ko, I. S.; Cho, M. H.; Kim, S. Design of a Hard X-Ray Beamline and End-Station for Pump and Probe Experiments at Pohang Accelerator Laboratory X-Ray Free Electron Laser Facility. *Nucl. Instrum. Methods Phys. Res., Sect. A* **2016**, *810*, 74−79.
(29) Tan, P. H.; Han, W. P.; Zhao, W. J.; Wu, Z. H.; Chang, K.; Wang, H.; Wang, Y. F.; Bonini, N.; Marzari, N.; Pugno, N.; Savini, G.; Lombardo, A.; Ferrari, A. C. The Shear Mode of Multilayer Graphene. *Nat. Mater.* **2012**, *11* (4), 294−300.
(30) Zhao, Y.; Luo, X.; Li, H.; Zhang, J.; Araujo, P. T.; Gan, C. K.; Wu, J.; Zhang, H.; Quek, S. Y.; Dresselhaus, M. S.; Xiong, Q. Interlayer Breathing and Shear Modes in Few-Trilayer MoS_2 and WSe_2. *Nano Lett.* **2013**, *13* (3), 1007−1015.
(31) Zhao, Y.; Luo, X.; Zhang, J.; Wu, J.; Bai, X.; Wang, M.; Jia, J.; Peng, H.; Liu, Z.; Quek, S. Y.; Xiong, Q. Interlayer Vibrational Modes in Few-Quintuple-Layer Bi_2Te_3 and Bi_2Se_3 Two-Dimensional Crystals: Raman Spectroscopy and First-Principles Studies. *Phys. Rev. B: Condens. Matter Mater. Phys.* **2014**, *90* (24), 245428.
(32) Glinka, Y. D.; Babakiray, S.; Johnson, T. A.; Holcomb, M. B.; Lederman, D. Acoustic Phonon Dynamics in Thin-Films of the Topological Insulator Bi_2Se_3. *J. Appl. Phys.* **2015**, *117* (16), 165703.
(33) Giraud, S.; Kundu, A.; Egger, R. Electron-Phonon Scattering in Topological Insulator Thin Films. *Phys. Rev. B: Condens. Matter Mater. Phys.* **2012**, *85* (3), 035441.
(34) Lifshitz, E. M. The Theory of Molecular Attractive Forces between Solids. *Perspect. Theor. Phys.* **1992**, *2* (1), 329−349.
(35) Delves, R. T.; Bowley, A. E.; Hazelden, D. W.; Goldsmid, H. J. Anisotropy of the Electrical Conductivity in Bismuth Telluride. *Proc. Phys. Soc., London* **1961**, *78* (5), 838−844.
(36) Matsuda, I.; Hasegawa, S. Fermiology and Transport in Metallic Monatomic Layers on Semiconductor Surfaces. *J. Phys.: Condens. Matter* **2007**, *19* (35), 355007.
(37) Lahoud, E.; Maniv, E.; Petrushevsky, M. S.; Naamneh, M.; Ribak, A.; Wiedmann, S.; Petaccia, L.; Salman, Z.; Chashka, K. B.; Dagan, Y.; Kanigel, A. Evolution of the Fermi Surface of a Doped Topological Insulator with Carrier Concentration. *Phys. Rev. B: Condens. Matter Mater. Phys.* **2013**, *88* (19), 195107.
(38) Yang, W. J.; Lee, C. W.; Kim, D. S.; Kim, H. S.; Kim, J. H.; Choi, H. Y.; Choi, Y. J.; Kim, J. H.; Park, K.; Cho, M. H. Tuning of Topological Dirac States via Modification of van Der Waals Gap in Strained Ultrathin Bi_2Se_3 Films. *J. Phys. Chem. C* **2018**, *122* (41), 23739−23748.
(39) Emin, D. *Polarons*; Cambridge University Press, 2012.
(40) Zhang, J.; Zhang, Y.; Wu, X.; Guan, R.; Li, J.; Gao, C.; Wang, Q.; Ma, Y.; Zhao, Z.; Liu, G. High-Pressure Topological Transport Study of Bi_2Se_3 Single Crystal. *Appl. Surf. Sci.* **2020**, *507*, 145052.

https://doi.org/10.1021/acs.nanolett.1c01424
Nano Lett. 2021, 21, 8554−8562